ADVANCED FUNCTIONAL MATERIALS
www.afm-journal.de

Strong Surface-Termination Effect on Electroresistance in Ferroelectric Tunnel Junctions

Hiroyuki Yamada, Atsushi Tsurumaki-Fukuchi, Masaki Kobayashi, Takuro Nagai, Yoshikiyo Toyosaki, Hiroshi Kumigashira, and Akihito Sawa*

Tunnel electroresistance in ferroelectric tunnel junctions (FTJs) has attracted considerable interest, because of a promising application to nonvolatile memories. Development of ferroelectric thin-film devices requires atomic-scale band-structure engineering based on depolarization-field effects at interfaces. By using FTJs consisting of ultrathin layers of the prototypical ferroelectric $BaTiO_3$, it is demonstrated that the surface termination of the ferroelectric in contact with a simple-metal electrode critically affects properties of electroresistance. $BaTiO_3$ barrier-layers with TiO_2 or BaO terminations show opposing relationships between the polarization direction and the resistance state. The resistance-switching ratio in the junctions can be remarkably enhanced up to 10^5% at room temperature, by artificially controlling the fraction of BaO termination. These results are explained in terms of the termination dependence of the depolarization field that is generated by a dead layer and imperfect charge screening. The findings on the mechanism of tunnel electroresistance should lead to performance improvements in the devices based on nanoscale ferroelectrics.

1. Introduction

Ferroelectric tunnel junctions (FTJs) show a nonvolatile change in junction resistance that depends on the direction of ferroelectric polarization; this effect, known as tunnel electroresistance (TER), can be utilized in nonvolatile memories.[1–13] TER-based memory systems have a simple structure of metal/ferroelectric/metal and they combine the advantages of both ferroelectric random-access-memory and oxide-based resistive-switching memory. They are therefore considered to provide a basis for the construction of nonvolatile memory systems with low power consumptions and large capacities.[14–16]

In general, charge conduction across an insulating barrier is sensitive to the interfacial electronic state at the electrode–insulator interface. The importance of the interface has also been pointed out for TER in FTJs. An earlier theory proposed that a finite charge-screening length at the electrode–ferroelectric interface generates a depolarization field that modulates the height of the tunneling barrier in a manner dependent on the direction of polarization.[17,18] The dielectric dead-layer also generates a depolarization field, causing TER.[19,20] These interfacial effects should depend not only on the combination of constituent materials, but also on local atomic structures at the interface. In fact, first-principles calculations on prototypical perovskite ferroelectrics (ABO_3) predicted a remarkable surface-termination dependence and suggest that the depolarization fields practically vanish at the interface between a simple metal and an *A*O-site-terminated ABO_3.[21] The studies imply that the surface termination of ABO_3 by either *A*O or BO_2 sites on the (001)-oriented surface will critically affect charge conduction in ferroelectric junctions. The role of surface-termination in perovskite has recently been the subject of an intensive investigation that concentrated on all-perovskite interfaces.[22,23] The termination issue has not, however, been examined for simple metal–ABO_3 interface except by few theoretical studies.[21,24] Experimental elucidation of the correlation between the microstructure of the interface and its transport properties is crucial for understanding charge conduction in ferroelectric junctions and for the development of TER-based memories.

We investigated electroresistance occurring in FTJs consisting of the prototypical ferroelectric $BaTiO_3$ (BTO) with controlled BaO (*A*-site) or TiO_2 (*B*-site) terminations, fabricated by a combination of epitaxial growth and ex situ surface treatment. We used Co/BTO/(La,Sr)MnO_3 (LSMO) junctions to elucidate the role of surface termination, because the functionalities of FTJs have previously been established by extensive studies on this heterostructure.[4–6]

Dr. H. Yamada, Dr. A. Tsurumaki-Fukuchi, Y. Toyosaki, Dr. A. Sawa
National Institute of Advanced Industrial Science and Technology (AIST)
Higashi 1–1–1, Tsukuba, Ibaraki 305-8562, Japan
E-mail: hiroyuki-yamada@aist.go.jp
Dr. H. Yamada
Japan Science and Technology Agency (JST)
PRESTO
Kawaguchi, Saitama 332-0012, Japan
Dr. M. Kobayashi, Prof. H. Kumigashira
Photon Factory
KEK
Oho 1–1, Tsukuba, Ibaraki 305-0801, Japan
Dr. T. Nagai
National Institute for Materials Science(NIMS)
Namiki 1–1, Tsukuba, Ibaraki 305-0044, Japan

DOI: 10.1002/adfm.201500371

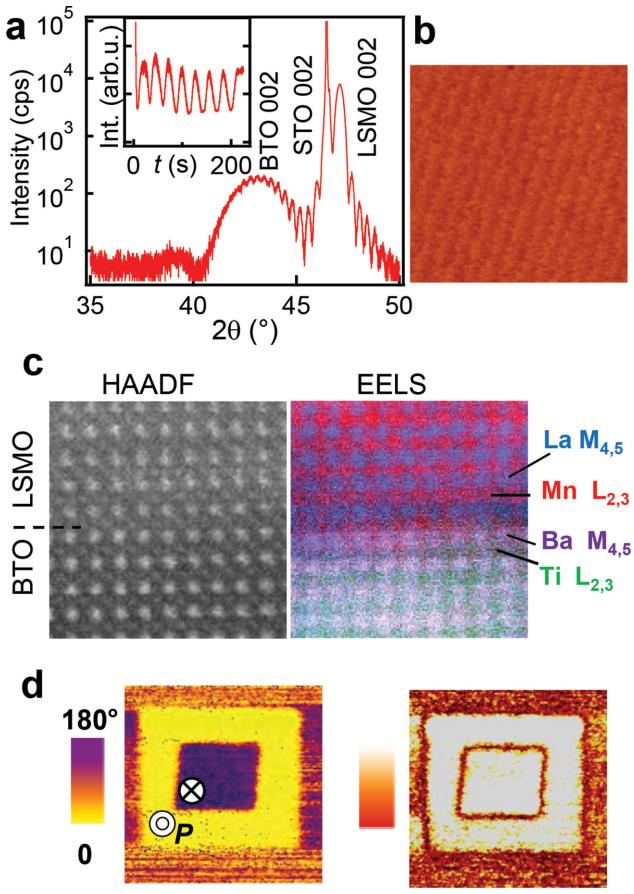

Figure 1. a) X-ray 2θ–ω scan of a heterostructure consisting of 8 u.c.-BTO and 80 u.c.-LSMO layers grown on STO. Inset: Intensity oscillations in reflection high-energy electron diffraction (RHEED) during the growth of BTO. b) AFM image (3×3 μm^2) of the surface of the BTO/LSMO heterostructure. c) Cross-sectional HAADF-STEM image of the BTO/LSMO interface combined with EELS mappings for La, Mn, Ba, and Ti. d) PFM phase (left) and amplitude (right) images of the BTO/LSMO heterostructure taken after writing the polarization (P) domains (1×1 μm^2 for P_{up}).

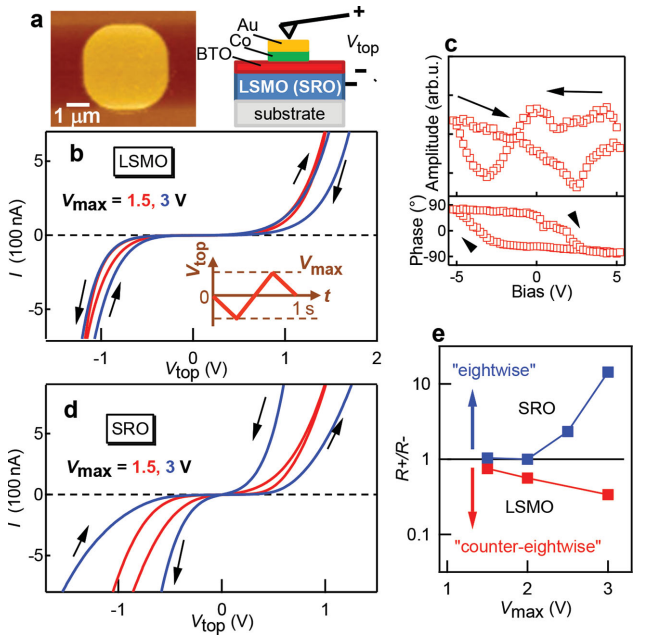

Figure 2. a) AFM topographic image and cross-sectional schematics of a single junction for I–V measurements with an AFM-based setup. b) I–V characteristics of Co/BTO(B)/LSMO junction. The "counter-eightwise" direction of hysteresis is shown by arrows. (Inset) Triangular-wave voltage applied to the AFM tip (V_{top}) for I–V measurement. c) Hysteresis curves of the PFM phase and amplitude for Co/BTO(B)/LSMO junction. d) I–V curves of Co/BTO(A)/SRO junction with an "eightwise" direction of hysteresis. e) Resistance-switching ratio evaluated at $V = +1$ V for Co/BTO(B)/LSMO and Co/BTO(A)/SRO junctions, plotted as a function of V_{max}. See the text for definitions of R^+ and R^-.

2. Results

2.1. Characterizations of BTO-Based FTJs

An ultrathin BTO film [eight unit cells (u.c.) thick (3.2 nm)] and an LSMO bottom-electrode layer (80 u.c. thick) were deposited in a layer-by-layer growth mode on a TiO_2 (B-site)-terminated $SrTiO_3$ (STO) (001) substrate (**Figure 1**a). Atomic force microscopy (AFM) confirmed that the film was atomically flat with step-and-terrace structures on its surface (Figure 1b). We observed the atomic arrangement of (La,Sr)O–MnO_2–BaO–TiO_2 at the BTO/LSMO interface by means of high-angle, annular, dark-field, scanning transmission-electron microscopy (HAADF-STEM) in combination with electron energy-loss spectroscopy (EELS) (Figure 1c). This showed predominant B-site termination at the interface, from which we expected B-site termination of the BTO surface. Ferroelectricity in the ultrathin BTO was confirmed by means of typical piezoresponse-force microscopy (PFM) observations on electrically written polarization domains with opposite directions (Figure 1d).

2.2. Electroresistance in BTO-Based FTJs

To get insights into natures of the TER phenomena in the BTO(B)-based FTJs, we investigated their current–voltage (I–V) characteristics, focusing on hysteresis appearing in the I–V curves. An Au/Co layered film was prepared by a lift-off method (**Figure 2**a). Figure 2b shows the I–V curves of a Co/B-site-terminated BTO [BTO(B)]/LSMO junction, measured by sweeping the voltage (V_{top}) on the probe in the pattern 0 V → $-V_{max}$ → $+V_{max}$ → 0 V (Inset, Figure 2b). The duration of one cycle of the I–V scan was 1 s. Note that we did not observe any abrupt resistance change or stochastic behavior as an indication of dielectric breakdown in the I–V curves (see Figure S1a, Supporting Information). The Co/BTO(B)/LSMO junction exhibited nonlinear I–V curves, indicating that the ultrathin BTO layer acts as a potential barrier for charge conduction (see Figure S1b–d, Supporting Information). The electroresistance appeared in a form of hysteretic behavior of the I–V curves for low-V_{top} regions. Magnitude of the electroresistance depended on V_{max}. A small hysteresis was observed when V_{max} was set to 1.5 V. Further increases in V_{max} up to 3 V resulted in markedly increased hysteresis. These features are consistent with those in the previous report on TER in the Co/BTO/LSMO FTJs, showing a continuous evolution of electroresistance with increasing writing voltage around 2–3 V.[4] We also observed typical PFM hysteresis loops of phase and amplitude (Figure 2c) in the Co/BTO/

LSMO junction, as previously reported.[4–6] Regarding the correlation between the ferroelectricity and electroresistance, we discuss later in Section 2.5.

2.3. "Sign" of Electroresistance in FTJs

We now discuss a direction of hysteresis in the *I*–*V* curves. In the Co/BTO(*B*)/LSMO junction, the hysteresis loop was always "counter-eightwise".[25] That is to say, the resistance state changed from a low-resistance state (LRS) to a high-resistance state (HRS) by applying a positive voltage on the Co electrode, whereas application of a negative voltage changed the resistance state from a HRS to a LRS. The applications of positive and negative V_{top} induces polarization pointing downward (toward the oxide bottom-electrode) and upward (toward the Co top-electrode), respectively. In the "counter-eightwise" Co/BTO(*B*)/LSMO junction, therefore, downward polarization stabilizes the HRS, as previous studies reported.[4,5,7]

To examine electroresistance in *A*-site-terminated BTO [BTO(*A*)], we fabricated the junctions with a $SrRuO_3$ (SRO) bottom electrode. It is well known that thermal instability of a RuO_2 surface results in SrO termination (*A*-site-termination) of SRO films,[26] thereby stabilizing *A*-site termination for BTO grown on SRO. As can be seen in Figure 2d, the Co/BTO(*A*)/SRO junction exhibited nonlinear and hysteretic *I*–*V* curves, similar to those observed with the Co/BTO(*B*)/LSMO junction. However, the Co/BTO(*A*)/SRO junction showed "eightwise" switching, indicating that the HRS occurs in upward polarization. Here, we define the resistance value at $V_{top} = +1$ V for the two branches in the hysteretic *I*–*V* curve measured during an increase in V_{top} from $-V_{max}$ to $+V_{max}$ as R^+ and that during a decrease in V_{top} from $+V_{max}$ to 0 V as R^-. Note that +1 V is smaller than the threshold voltage (≈1.5 V) of the resistive switching. The switching ratio (R^+/R^-) was plotted as a function of V_{max} (Figure 2e). Note that the value of R^+/R^- is less than 1 for the counter-eightwise switching in the Co/BTO(*B*)/LSMO junction.

The difference in the "sign" of electroresistance between the Co/BTO(*A*)/SRO and Co/BTO(*B*)/LSMO junctions suggests that the electroresistance in FTJs depends on the surface-termination at the interfaces. To evaluate the role of the bottom-interface (BTO/oxide), we fabricated an FTJ consisting of an *A*-site-terminated LSMO [LSMO(*A*)] bottom electrode deposited on an SRO buffer layer (see Figures S2a–d, Supporting Information). The Co/BTO(*A*)/LSMO(*A*) junction showed "eightwise" switching (Figures S2e, Supporting Information), as observed for Co/BTO(*A*)/SRO junction. This result shows that the type of bottom-electrode oxide does not affect the direction of hysteresis in the *I*–*V* curves.

2.4. Surface-Termination Control for Ultrathin BTO Layers

To explore the role of the top interface (Co/BTO) exclusively, we fabricated *A*-site-terminated BTO barrier layers on LSMO(*B*) bottom electrodes. A general approach for obtaining *A*-site termination is growth of rock-salt SrO_x ($x \approx 1$) on a *B*-site-terminated surface.[22] We used this technique and grew an ultrathin (1 u.c.) BaO_x layer on a BTO(*B*)/LSMO heterostructure (see

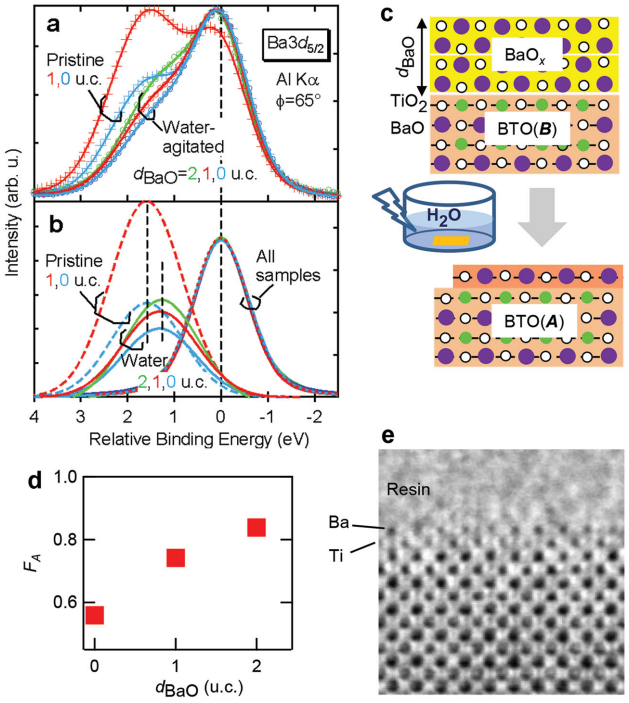

Figure 3. a) XPS spectra for Ba $3d_{5/2}$ core-level for pristine and water-agitated BaO_x/BTO/LSMO heterostructures with BaO_x thicknesses (d_{BaO}) of 0 (BTO/LSMO), 1, or 2 u.c., together with fitted curves. b) Main peaks (bulk contribution with relative binding energy = 0), and subpeaks (surface contributions with relative binding energy >0, marked by broken lines) in Ba $3d_{5/2}$ spectra, deduced from fitting to (a). c) Schematic representations of the effects of agitation in water on the BTO surface. d) Fraction of *A*-site-termination (*FA*) plotted against d_{BaO} for water-agitated heterostructures, estimated from the normalized intensity of the subpeaks (solid curves in b) and from Figure S2d (Supporting Information). e) BF-STEM image of the water-agitated heterostructure (d_{BaO} = 2 u.c.).

Figures S3a–d, Supporting Information). The BaO_x/BTO(*B*)/LSMO heterostructure was characterized by means of x-ray photoemission spectroscopy (XPS). We focused on the Ba 3*d* core level, the binding energy of which is very sensitive to the environment.[27,28] Under surface-sensitive conditions [a higher emission-angle (ϕ) of 65°], the heterostructure with a 1 u.c. BaO_x layer on BTO exhibited two peaks separated by 1.6 eV in the Ba $3d_{5/2}$ core level (**Figure 3**a,b). The higher-binding-energy component was attributed to the topmost surface, because it was suppressed at a normal emission angle ($\phi = 0°$) (Figure S3d, Supporting Information). A surface contribution was also observed, in the BTO(*A*)/LSMO(*A*) heterostructure, but its chemical shift, i.e., the relative binding energy of the subpeak (surface contribution) with respect to the main peak (bulk contribution), was 1.3 eV (Figure S2d, Supporting Information). This disagreement suggests that deposition of alkali-earth oxide alone does not convert the *B*-site termination into *A*-site termination.[29] In fact, ultrasonic agitation in water markedly decreased the intensity of the subpeak, indicating that the topmost layer consisted of BaO_x, which is water soluble. However, we observed another subpeak as a result of water agitation, and we found that its relative binding energy was shifted to 1.3 eV. We also confirmed that the water-agitated samples showed

excellent flatness (Figure S3c, Supporting Information). These results indicate that agitation in water converted the rock-salt BaO_x (biatomic layer) into an *A*-site-terminated surface for BTO (single-atomic layer) by removing extra atoms from the surface (Figure 3c).

The relative area of the subpeak, i.e., the fraction of the *A*-site-termination area (F_A) for the water-agitated samples, increased monotonously with the thickness of the deposited BaO_x (d_{BaO}), as shown in Figure 3b. We estimated F_A from a comparison with BTO(*A*)/LSMO(*A*), and this was plotted as a function of d_{BaO} (Figure 3d). This revealed that the *A*-site-termination is quite dominant for $d_{BaO} = 2$ u.c. ($F_A > 0.8$), which was confirmed by means of bright-field (BF) – STEM (Figure 3e). It is also noted that, despite the presence of a step-and-terrace surface (Figure 1b), the pristine BTO(*B*)/LSMO heterostructure ($d_{BaO} = 0$) contained a small amount of BaO_x on the surface, appearing as a 1.6 eV chemical shift in the XPS spectra (Figure 3b). In this heterostructure, the *A*-site-termination (1.3 eV chemical shift) was negligible. Surface segregation of BaO_x has been reported in a single-crystal study that demonstrated the evolution of surface reconstructions having a Ti-enriched structure.[30] Native BaO_x similarly undergoes conversion of *B*-site termination into partly *A*-site termination ($F_A \approx 0.5$) on agitation in water. We also confirmed that rock-salt BaO_x does not induce electroresistance (Figure S3e, Supporting Information).

2.5. Impact of Surface-Termination Engineering on Electroresistance

An impact of the change in surface termination was detected from the sign (the direction of the hysteresis) and the magnitude of electroresistance. **Figure 4**a presents *I*–*V* curves measured with $V_{max} = 5$ V for termination-engineered Co/BTO(*A*)/LSMO junctions having various values of F_A. The junctions showed a remarkable "eightwise" switching, indicating that LRS (HRS) occurs with downward (upward) polarization. The improved F_A increased resistance at HRS (R_H) and decreased

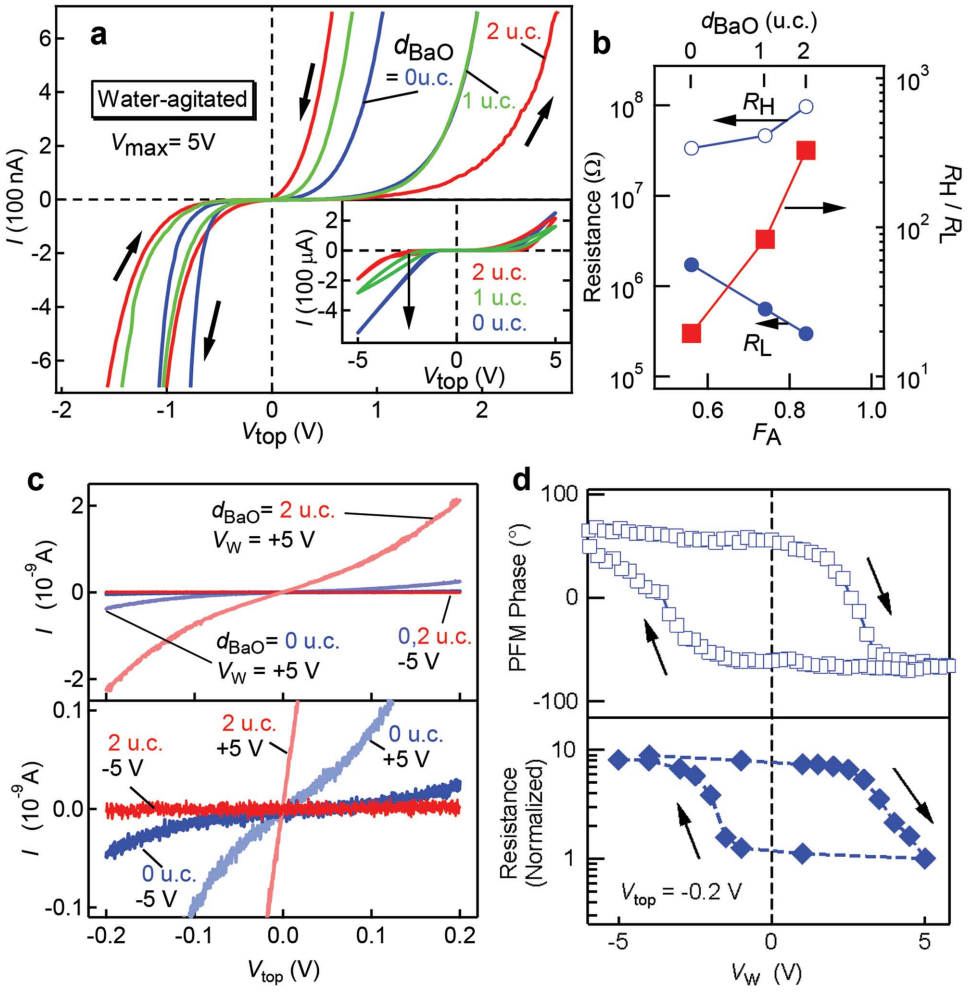

Figure 4. a) *I*–*V* curves ($V_{max} = 5$ V) of Co/BTO(*A*)/LSMO junctions fabricated with water-agitated BaO_x/BTO for $d_{BaO} = 0$, 1, or 2 u.c. (Inset) Data shown in full range. b) Resistances in HRS and LRS (R_H, and R_L, respectively) evaluated at $V = +1$ V and resistance-switching ratio R_H/R_L value, plotted against F_A and d_{BaO}. c) *I*–*V* curves in HRS and LRS ($V_{max} = 0.2$ V) of the termination-engineered junctions ($d_{BaO} = 0$ or 2 u.c.) measured after applications of writing voltage ($V_w = +5$ or –5 V). The bottom panel shows a magnified view of the *I*–*V* curves near zero current. d) Hysteresis curves of PFM phase (top) and normalized resistance (bottom) measured after applications of writing voltage V_w for the junction ($d_{BaO} = 0$ u.c.).

resistance at LRS (R_L), leading to a substantial increase in the resistance-switching ratio R_H/R_L (Figure 4b). For the junction with d_{BaO} = 2 u.c. ($F_A \approx 0.8$) the R_H/R_L estimated from I values at V_{top} = +1 V was as high as 330. From the analysis of the I–V curves in positive V_{top} bias (Figures S1, Supporting Information), the barrier-height (Φ_B)-changes between HRS and LRS were estimated to be 147, 136, and 87 meV, for d_{BaO} = 2, 1, 0 u.c., respectively. These results prove that the sign and magnitude of electroresistance are dominated by surface-termination at the Co/BTO interface.

The electroresistence in our termination-engineered junctions also exhibited nonvolatile features, as generally observed in FTJs. Figure 4c presents I–V curves (V_{max} = 0.2 V) of the Co/BTO(A)/LSMO junctions after applications of writing voltage (V_W = ±5 V). An application of V_W was performed by voltage sweeping (0 V → V_W → 0 V) in 0.1 s. For both d_{BaO} = 0 and 2 u.c., the positive and negative V_W caused an LRS and HRS, respectively, as expected from the "eightwise" switching (Figure 4a). In the LRS (HRS), the junction resistance for d_{BaO} = 2 u.c. was much lower (higher) than that for d_{BaO} = 0 u.c. for entire voltage region, which is consistent with the results in Figure 4b. Magnitude of the nonvolatile electroresistance (R_H/R_L), which was evaluated from I-values at V_{top} = –0.2 V in Figure 4c, was 8.2 for d_{BaO} = 0 u.c. For d_{BaO} = 2 u.c., the switching ratio was increased to (1.4 ± 0.1) × 10^3, which is comparable with the highest value reported so far on the Co/BTO/LSMO FTJs.[6] Figure 4d displays V_w-dependence of junction resistance (V_{top} = –0.2 V) for the Co/BTO(A)/LSMO junction (d_{BaO} = 0 u.c.). Transitions between the LRS and HRS occurred around V_W = ±3 V. At these voltages, we observed the polarization-reversal of the BTO barrier by means of PFM hysteresis measurement for the same FTJ (Figure 4d, top panel), indicating that the polarization reversal is involved in the nonvolatile electroresistance.

3. Discussion

Our results demonstrate that the electroresistance in the BTO-based FTJs is very sensitive to the BTO surface. One may concern about the contribution of unintentionally-formed Co-oxide layer to the electroresistance. However, in FTJs consisting of chemically more inert Pt electrode (see Figure S4, Supporting Information), the signs of the electroresistance of Pt/BTO(B)/LSMO and Pt/BTO(A)/SRO coincided with those of FTJs consisting of the Co top-electrodes [Co/BTO(B)/LSMO (Figure 2b) and Co/BTO(A)/SRO (Figure 2d)], respectively. We also note that no forming process was needed to obtain stable resistive switching in our devices, which is distinct from conventional resistive switching based on redox reactions of metal oxides. From these observations, the surface termination can be considered to be a main determinant of the sign of electroresistance in the BTO-based FTJs.

Here, we discuss a possible mechanism of the surface-termination-dependent electroresistance in the BTO-based FTJs in terms of the surface-termination-dependent local ferroelectricity and the dielectric response at the BTO interfaces, as predicted by the first-principles calculations.[21] Possible energy-band diagrams for the BTO(A) and BTO(B) junctions are shown in **Figure 5**. (see also Figure S5, Supporting Information

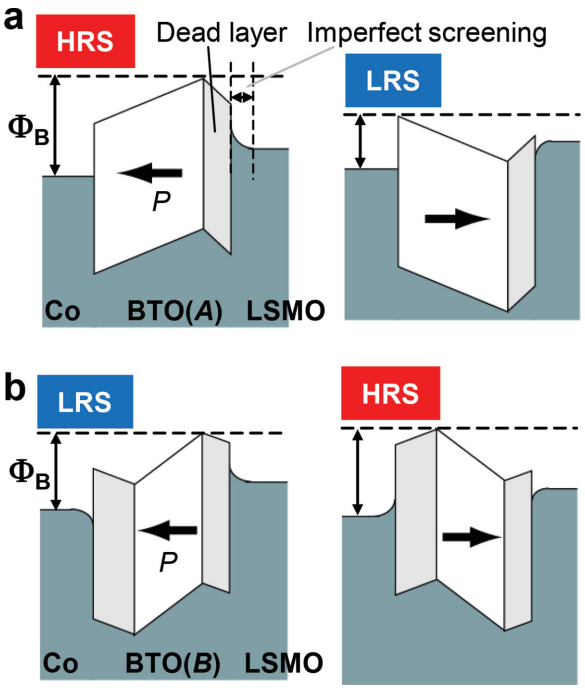

Figure 5. a,b) Schematic representations of the energy-band diagram for Co/BTO(A)/LSMO and Co/BTO(B)/LSMO junctions with two opposite directions of polarization, which explain the relationship between the direction of polarization (P) (arrows) and the resistance state (HRS or LRS).

for energetic band alignments of the constituent materials). We take into account two interfacial effects that are responsible for the polarization-dependent barrier height in electroresistance. The first of these effects is imperfect charge screening, as described by a finite screening length λ_{eff}, i.e., by band bending in an electrode.[17,18] The second effect is the presence of a dead layer in the ferroelectric barrier, creating an asymmetric potential distribution through formation of a depolarization field.[19,20,31,32] In the Co/BTO(A)/LSMO junction (Figure 5a), we consider practically perfect charge screening ($\lambda_{eff} \approx 0$) and a zero thickness of the dead layer at the Co/BTO(A) interface, as predicted theoretically.[21] In this case, the dead layer at the BTO(A)/LSMO interface is exclusively responsible for the polarization-dependent barrier height. The barrier height decreases when the polarization is oriented toward LSMO. This is consistent with the sign of electroresistance observed in the Co/BTO(A)/LSMO junctions. In Co/BTO(B)/LSMO (Figure 5b), on the contrary, the TiO_2 termination of the BTO surface causes the λ_{eff} and the dead layer at the Co/BTO(B) interface, which may surpass those at the BTO(B)/LSMO interface. In such junctions, the barrier height increases when the polarization points downward (toward LSMO) because a larger potential change at the Co/BTO(B) interface dominates the polarization-dependent barrier modulation.

Previous studies on FTJs with Co/BTO [or Pb(Zr,Ti)O_3]/LSMO heterostructures generally reported HRS (LRS) in downward (upward) polarization,[4,5,7,11] in agreement with the "counter-eightwise" switching, as shown in Figure 2b. However, the reverse relationship (HRS in upward polarization) has been observed in the Co/BTO/LSMO FTJ.[6] The change in the sign

of the TER for similar junctions can be explained in terms of competition between the two surface states.

4. Conclusion

We demonstrated that the electroresistance in BTO-based FTJs strongly depends on the surface terminations of the BTO ferroelectric barriers in contact with the metal electrode. The results are attributable to surface-termination-dependent interface ferroelectricity, which is also expected to occur in other perovskite ferroelectrics.[21] Thus surface-termination engineering of ferroelectrics, as a method for controlling charge conduction should be applicable to various types of FTJs.[8–13] Our findings provide a clue to understanding the microscopic and universal mechanism of ferroelectricity-controlled conduction in ferroelectric junctions, and should contribute to the development of the next-generation nonvolatile devices.

5. Experimental Section

Fabrication of Samples: Oxide films were fabricated by pulsed-laser deposition using a KrF excimer laser. The LSMO bottom-electrode layer was grown at a substrate temperature (T_{sub}) of 750 °C and an oxygen pressure (P_{O2}) of 0.1 Pa. The SRO bottom-electrode layer was deposited at T_{sub} = 600 °C and P_{O2} = 7 Pa on a $DyScO_3$ (110) substrate. BTO barrier layers were subsequently deposited at T_{sub} = 650 °C and P_{O2} = 4.5 Pa. BaO_x layers were deposited at T_{sub} = 600 °C and P_{O2} = 4.5 Pa. After the depositions, the heterostructures were cooled slowly in an atmosphere of oxygen (P_{O2} = 10 Pa). Water-agitated films were prepared by ultrasonic agitation of the (BaO_x)/BTO/LSMO films in deionized water for 10 min under an atmosphere of air.

XPS Measurements: XPS spectra were measured at room temperature using monochromatized Al Kα (1486.6 eV) radiation from an MX650 source (VG Scienta) as the incident x-rays. The photoelectrons were analyzed with an R3000 analyzer (VG Scienta). The Ba 3*d* levels were fitted by assuming two Voigt functions.

Electrical Measurements: Current–voltage (*I–V*) characteristics of the junctions were measured at room temperature by using AFM (MFP-3D; Asylum Research) operated in the conductive-tip (CT-AFM) mode using conductive cantilevers (Ti/Ir-coated silicon [Asyelec-01; Asylum Research]). The cantilever holder for CT-AFM was equipped with *I/V* amplifiers (ORCA, Dual Gain; Asylum Research), with different measurable current ranges.

PFM Measurements: The PFM responses of the BTO films were measured by using the AFM (MFP-3D) operated in its dual alternating current (AC) resonance tracking mode at typical resonance frequencies of ≈300 kHz. Piezoresponses were measured by applying AC driving voltages of 0.7–1.0 V. During the piezoelectric-hysteresis-loops measurement, DC bias voltage was removed to minimize the effects of electrostatic interactions.

STEM Measurements: Samples were mechanically cut and thinned by Ar-ion milling to give electron-transparent specimens. The measurement was performed by using a Titan^3 transmission electron microscope (FEI) operated at an acceleration voltage of 300 kV and fitted with a spherical aberration corrector (DCOR; CEOS GmbH). EELS spectrum imaging was conducted with a GIF Quantum 966 EELS spectrometer (Gatan Inc.) at a probe current of 50 pA and a collection semiangle of 73 mrad.

Supporting Information

Supporting Information is available from the Wiley Online Library or from the author.

Acknowledgements

We thank H. Nakao, K. Horiba, I. H. Inoue, and S. Ishibashi for useful discussions. We also thank Y. Sasaki, K. Moriyama, and K. Nayuki for preliminary TEM studies. Part of this work was financially supported by the JSPS KAKENHI (Grant No. 26286055), and technically supported by the "Nanotechnology Platform" (Grant No. A-14-NM-0075) of MEXT, Japan.

Received: January 29, 2015
Revised: February 25, 2015
Published online: March 24, 2015

[1] P. Maksymovych, S. Jesse, P. Yu, R. Ramesh, A. P. Baddorf, S. V. Kalinin, *Science* **2009**, *324*, 1421.
[2] A. Gruverman, D. Wu, H. Lu, Y. Wang, H. W. Jang, C. M. Folkman, M. Y. Zhuravlev, D. Felker, M. Rzchowski, C.-B. Eom, E. Y. Tsymbal, *Nano Lett.* **2009**, *9*, 3539.
[3] V. Garcia, S. Fusil, K. Bouzehouane, S. Enouz-Vedrenne, N. D. Mathur, A. Barthélémy, M. Bibes, *Nature* **2009**, *460*, 81.
[4] A. Chanthbouala, A. Crassous, V. Garcia, K. Bouzehouane, S. Fusil, X. Moya, J. Allibe, B. Dlubak, J. Grollier, S. Xavier, C. Deranlot, A. Moshar, R. Proksch, N. D. Mathur, M. Bibes, A. Barthélémy, *Nat. Nanotechnol.* **2012**, *7*, 101.
[5] A. Chanthbouala, V. Garcia, R. O. Cherifi, K. Bouzehouane, S. Fusil, X. Moya, S. Xavier, H. Yamada, C. Deranlot, N. D. Mathur, M. Bibes, A. Barthélémy, J. Grollier, *Nat. Mater.* **2012**, *11*, 860.
[6] D. J. Kim, H. Lu, S. Ryu, C.-W. Bark, C.-B. Eom, E. Y. Tsymbal, A. Gruverman, *Nano Lett.* **2012**, *12*, 5697.
[7] H. J. Mao, P. X. Miao, J. Z. Cong, C. Song, B. Cui, J. J. Peng, F. Li, G. Y. Wang, Y. G. Zhao, Y. Sun, L. R. Xiao, F. Pan, *J. Appl. Phys.* **2014**, *116*, 053703.
[8] Z. Wen, C. Li, D. Wu, A. Li, N. Ming, *Nat. Mater.* **2013**, *12*, 617.
[9] H. Yamada, V. Garcia, S. Fusil, S. Boyn, M. Marinova, A. Gloter, S. Xavier, J. Grollier, E. Jacquet, C. Carrétéro, C. Deranlot, M. Bibes, A. Barthélémy, *ACS Nano* **2013**, *7*, 5385.
[10] Z. Wen, L. You, J. Wang, A. Li, D. Wu, *Appl. Phys. Lett.* **2013**, *103*, 132913.
[11] D. Pantel, S. Goetze, D. Hesse, M. Alexe, *Nat. Mater.* **2012**, *11*, 289.
[12] L. Jiang, W. S. Choi, H. Jeen, S. Dong, Y. Kim, M.-G. Han, Y. Zhu, S. V. Kalinin, E. Dagotto, T. Egami, H. N. Lee, *Nano Lett.* **2013**, *13*, 5837.
[13] A. Crassous, V. Garcia, K. Bouzehouane, S. Fusil, A. H. G. Vlooswijk, G. Rispens, B. Noheda, M. Bibes, A. Barthélémy, *Appl. Phys. Lett.* **2010**, *96*, 042901.
[14] N. Setter, D. Damjanovic, L. Eng, G. Fox, S. Gevorgian, S. Hong, A. Kingon, H. Kohlstedt, N. Y. Park, G. B. Stephenson, I. Stolitchnov, A. K. Taganstev, D. V. Taylor, T. Yamada, S. Streiffer, *J. Appl. Phys.* **2006**, *100*, 051606.
[15] R. Waser, R. Dittmann, G. Staikov, K. Szot, *Adv. Mater.* **2009**, *21*, 2632.
[16] V. Garcia, M. Bibes, *Nat. Commun.* **2014**, *5*, 1.
[17] M. Y. Zhuravlev, R. F. Sabirianov, S. S. Jaswal, E. Y. Tsymbal, *Phys. Rev. Lett.* **2005**, *94*, 246802.
[18] D. Pantel, M. Alexe, *Phys. Rev. B* **2010**, *82*, 134105.
[19] M. Y. Zhuravlev, Y. Wang, S. Maekawa, E. Y. Tsymbal, *Appl. Phys. Lett.* **2009**, *95*, 052902.
[20] P. Sun, Y. Z. Wu, T. Y. Cai, S. Ju, *Appl. Phys. Lett.* **2011**, *99*, 052901.
[21] M. Stengel, D. Vanderbilt, N. A. Spaldin, *Nat. Mater.* **2009**, *8*, 392.
[22] A. Ohtomo, H. Y. Hwang, *Nature* **2004**, *427*, 423.
[23] N. Reyren, S. Thiel, A. D. Caviglia, L. Fitting Kourkoutis, G. Hammerl, C. Richter, C. W. Schneider, T. Kopp, A.-S. Rüetschi,

D. Jaccard, M. Gabay, D. A. Muller, J.-M. Triscone, J. Mannhart, *Science* **2007**, *317*, 1196.
[24] L. Shen, T. Zhou, Z. Bai, M. Zeng, J. Q. Goh, Z.-M. Yuan, G. Han, B. Liu, Y. P. Feng, *Phys. Rev. B.* **2012**, *85*, 064105.
[25] R. Muenstermann, T. Menke, R. Dittmann, R. Waser, *Adv. Mater.* **2010**, *22*, 4819.
[26] G. Koster, L. Klein, W. Siemons, G. Rijnders, J. S. Dodge, C.-B. Eom, D. H. A. Blank, M. R. Beasley, *Rev. Mod. Phys.* **2012**, *84*, 253.
[27] L. T. Hudson, R. L. Kurtz, S. W. Robey, D. Temple, R. L. Stockbauer, *Phys. Rev. B* **1993**, *47*, 10832.
[28] H. Kumigashira, K. Horiba, H. Ohguchi, K. Ono, M. Oshima, N. Nakagawa, M. Lippmaa, M. Kawasaki, H. Koinuma, *Appl. Phys. Lett.* **2003**, *82*, 3430.
[29] T. Ohsawa, R. Shimizu, K. Iwaya, T. Hitosugi, *ACS Nano* **2014**, *8*, 2223.
[30] A. M. Kolpak, D. Li, R. Shao, A. M. Rappe, D. A. Bonnel, *Phys. Rev. Lett.* **2008**, *101*, 036102.
[31] A. Tsurumaki-Fukuchi, H. Yamada, A. Sawa, *Appl. Phys. Lett.* **2013**, *103*, 152903.
[32] A. Tsurumaki, H. Yamada, A. Sawa, *Adv. Funct. Mater.* **2012**, *22*, 1040.